Society of Medical Education & Research

2022, Volume 2, Issue 2, Page No: 89-110
ISSN: 3108-4826

Journal of Medical Sciences and Interdisciplinary Research

STAB1⁺ Macrophages Drive Immunosuppressive Efferocytosis in Colon Adenocarcinoma: Insights from Integrated Histopathologic and Transcriptomic Analysis

Andreas Nikolaus Schmid[1]*, Lukas Ferdinand Keller[1]

[1]Department of Management, School of Economics, University of Regensburg, Regensburg, Germany.

***E-mail** ✉ a.schmid.regensburg@outlook.com

Abstract

Colon adenocarcinoma (COAD) shows poor responsiveness to immunotherapy largely because its tumor microenvironment (TME) is immunologically "cold." Efferocytosis plays a critical role in shaping the TME; however, its underlying mechanisms and clinical relevance in COAD remain poorly understood. We integrated transcriptomic data, histopathological images, and clinical information from 387 patients with COAD. Image features were derived using ResNet50 and CellProfiler, and a multimodal machine learning model was then developed to assess prognostic risk. In addition, bulk RNA sequencing, single-cell RNA sequencing, and spatial transcriptomics were jointly analyzed to systematically delineate efferocytosis-related immune cell populations and their associated signaling pathways. The efferocytosis-driven risk model showed robust prognostic accuracy at multiple time points and functioned independently of established clinical factors. From a mechanistic perspective, we identified a population of STAB1⁺ tumor-associated macrophages (TAMs) that was enriched in COAD tumors and characterized by elevated efferocytosis capacity, M2-like polarization, and activation of mTORC1 signaling. In vitro experiments demonstrated that STAB1 was required for IL-4–mediated M2 polarization, and that suppressing STAB1 reduced the development of immunosuppressive TAMs. Analyses using single-cell and spatial transcriptomics further indicated that this macrophage subset was transcriptionally distinct and became more abundant after neoadjuvant treatment. This work presents a multimodal prognostic framework that combines histopathological image analysis with molecular data, and for the first time highlights the central role of STAB1⁺ tumor-associated macrophages in driving an immunosuppressive tumor microenvironment through efferocytosis and mTORC1 signaling. Our results offer a clinically relevant tool for risk stratification as well as a promising therapeutic target. Inhibiting STAB1 may help expand the effectiveness of immunotherapy in COAD patients who show poor responses to immune checkpoint inhibitors.

Keywords: Tumor-associated, Macrophages deep learning, STAB1, Colon adenocarcinoma, Histopathology, Efferocytosis

Introduction

Colorectal cancer (CRC), comprising malignancies of both the colon and rectum, ranks as the second leading contributor to cancer-related deaths worldwide [1]. Colon adenocarcinoma (COAD) constitutes the most common anatomical form of CRC and has demonstrated a notable upward trend in incidence, particularly among younger individuals. Because early-stage disease often lacks clear clinical symptoms, many patients are diagnosed only after the tumor has progressed to an advanced stage, greatly reducing the feasibility of curative surgical resection [2-4]. Although therapeutic strategies for COAD—including chemotherapy, radiotherapy, molecularly targeted agents, and immune checkpoint inhibitors (ICIs) [5, 6]—have expanded considerably, their benefits remain limited in patients with microsatellite-stable (MSS) tumors [7, 8]. In addition, treatment-related toxicity and the emergence of drug resistance continue to undermine long-term disease control, presenting major clinical challenges [9, 10].

Access this article online https://smerpub.com/

Received: 27 May 2022; **Accepted:** 16 September 2022

How to cite this article: Schmid AN, Keller LF. STAB1⁺ Macrophages Drive Immunosuppressive Efferocytosis in Colon Adenocarcinoma: Insights from Integrated Histopathologic and Transcriptomic Analysis. J Med Sci Interdiscip Res. 2022;2(2):89-110. https://doi.org/10.51847/4Peiu63ffW

A growing body of evidence indicates that the colon adenocarcinoma tumor microenvironment (TME) is largely noninflamed or "cold," marked by weak tumor antigen presentation, poor recruitment of effector T lymphocytes, and a predominance of immunosuppressive myeloid cell populations, especially tumor-associated macrophages (TAMs) [11-15]. These features collectively contribute to immune escape and reduce responsiveness to immunotherapeutic approaches. Among the mechanisms driving immune suppression within the TME, efferocytosis—the clearance of apoptotic cells by macrophages—has emerged as a critical regulatory process [16, 17]. This process dampens antitumor immunity by limiting tumor-associated antigen (TAA) availability, skewing macrophages toward an M2-like phenotype, and activating downstream immunosuppressive signaling pathways, thereby promoting tumor growth and metastatic dissemination [18-20].

Despite its therapeutic potential, translating efferocytosis-targeted strategies into clinical practice is hindered by difficulties in identifying suitable patient populations. In particular, routine implementation of large-scale transcriptomic profiling is constrained by high costs, limited accessibility, and significant operational demands.

Advances in computational statistics and machine learning are increasingly enabling individualized cancer management [21-23]. At the same time, innovations in digital pathology have created new possibilities for extracting clinically meaningful information from standard diagnostic materials [24-27]. By combining deep learning–based analysis of hematoxylin and eosin (H&E)–stained slides with traditional image processing methods, it is now possible to derive biologically informative features from routine histopathological images, supporting improved disease classification and prognostic assessment [28-30]. In this study, we assembled a comprehensive dataset comprising histopathological images, transcriptomic profiles, and clinical records from 387 patients with COAD. Using ResNet50 and CellProfiler, we extracted multi-resolution image features and constructed an efferocytosis-associated multimodal risk model through systematic evaluation of 100 machine learning algorithm combinations. This approach bridges molecular-level insights with practical clinical implementation, yielding strong prognostic performance and enhanced patient stratification.

To further elucidate the cellular and spatial basis of efferocytosis-driven immunosuppression, we integrated single-cell RNA sequencing (scRNA-seq) with spatial transcriptomic analyses. This strategy enabled detailed characterization of immune cell subpopulations and their spatial organization within tumors. Notably, we identified a distinct subset of $STAB1^{+}$ macrophages preferentially localized to tumor regions, which exhibited pronounced immunosuppressive properties and a strong bias toward M2-like polarization. In addition, leveraging single-cell transcriptomic data from neoadjuvant-treated COAD samples, we systematically examined how different therapeutic interventions reshape the efferocytosis-related immune landscape. Together, these findings provide new insights into therapy-induced immune remodeling and deepen our understanding of immune regulatory mechanisms in colon adenocarcinoma.

Materials and Methods

Quality control and slide acquisition

From the TCGA-COAD cohort, 833 diagnostic whole-slide images (WSIs) of formalin-fixed, paraffin-embedded (FFPE) tissue were curated for analysis. These images were downloaded from the Genomic Data Commons (GDC) portal (https://portal.gdc.cancer.gov/) using the GDC Data Transfer Tool, with duplicate files and non-tumor control slides removed beforehand. Scanned at either 20× or 40× magnification, all slides were stored in SVS format.

Tile generation and tissue detection

WSIs were processed with OpenSlide (v3.4.1), and tissue regions were automatically identified in Python 3.8 using Histolab (v0.7.0) through adaptive Otsu thresholding applied in the HSV color space. To ensure continuous tissue coverage, masks were expanded using a 3 × 3 kernel and small gaps under 1 × 10^3 μm^2 were filled. From these tissue regions, non-overlapping 512 × 512-pixel tiles were generated. Tiles were excluded if they contained less than 60% tissue or showed over 20% artifacts, including folds or pen marks.

Feature extraction from pathological tiles

For each whole-slide image, residual tiles were analyzed using a ResNet-50 model pretrained on ImageNet to obtain high-level image features. In parallel, CellProfiler 4.2.4 was employed with two custom pipelines to extract

detailed cellular and tissue characteristics. The pipelines first separated eosin stains and hematoxylin using color unmixing, followed by segmentation of nuclei through adaptive thresholding and refinement with the watershed algorithm. Cytoplasmic and stromal regions were then approximated using propagation-based methods. From these segmented compartments, a variety of features were measured, including intensity metrics (such as mean and Haralick textures, median optical density), nuclear morphology (solidity, eccentricity, area), and spatial organization (nearest neighbor distances, Moran's I). The resulting feature sets were saved as CSV files and standardized via Z-score normalization across the cohort before being combined with bulk RNA-seq data.

Gene program association and feature refinement

RNA sequencing data (in transcripts per million, TPM, units) were downloaded from the Genomic Data Commons (GDC) repository of The Cancer Genome Atlas (TCGA). Enrichment scores for predefined hallmark pathways were generated for each individual sample via single-sample gene set enrichment analysis (ssGSEA) implemented in the GSVA R package (version 1.46.0). Non-parametric Spearman rank correlations were performed to assess associations between individual pathological variables and pathway enrichment scores. Only those variables demonstrating statistically significant correlations ($p < 0.05$) were carried forward into prognostic modeling. Additional feature pruning was achieved through elastic net penalty regression (using the glmnet package with mixing parameter $\alpha = 0.2$) to prioritize stable, minimally correlated predictors.

Survival modelling

Cases with recorded overall survival (OS) times and censoring information were randomly allocated to discovery and testing cohorts using an 80:20 split. Initial screening of candidate predictors was conducted via univariate Cox proportional hazards models, retaining only those with $p < 0.05$. Selected predictors were then fed into the MIME1 pipeline to build a composite risk stratification score. An extensive panel of machine learning algorithms was screened, with the ultimate prognostic model constructed by integrating bidirectional stepwise Cox regression (StepCox[both]) with random survival forest (RSF). Performance of the derived risk scores was independently verified in the held-out cohort, where discrimination was measured using time-dependent receiver operating characteristic area under the curve (AUC) and Harrell's concordance index (C-index) at the 1-, 3-, and 5-year landmarks.

Correlation of gene modules and hub gene identification

To explore the relationship between model-derived features and immune-related gene expression, Spearman correlation analyses were conducted. Significant associations were mapped as network diagrams using the ggraph package, and genes with the highest connectivity (degree centrality) were designated as hub genes for further functional analysis.

Bulk RNA-seq data and collection of single-cell

Publicly available scRNA-seq data were retrieved from the Gene Expression Omnibus (GEO; accession GSE161277), while bulk RNA-seq data were sourced from the TCGA-COAD cohort. Spatial transcriptomic profiles for colon cancer samples were accessed via the BioProject database (accession OEP001756).

In parallel, we generated novel scRNA-seq datasets from five COAD tumors resected after various neoadjuvant therapies: (1) chemotherapy only, (2) chemotherapy combined with PD-1 blockade, (3) chemoradiotherapy, (4) chemotherapy plus bevacizumab, and (5) untreated controls. All samples were processed and sequenced following BGI Genomics' standard protocols.

Data preprocessing and quality assurance

Single-cell gene expression datasets were processed using the Seurat package (version 4.2.0) in R (version 4.4.0). Rigorous quality filtering was implemented: cells exhibiting fewer detected genes, elevated mitochondrial content (>30%), or suspected multiplets (detected via DoubletFinder) were removed. Background ambient RNA was removed using SoupX. Expression values were subsequently normalized, log-transformed, and scaled across cells. Highly variable features were identified to drive downstream dimensionality reduction. Integration across batches was performed with Harmony to produce a unified dataset suitable for further investigation.

Identification of differentially expressed genes and functional enrichment

Differentially expressed genes (DEGs) were detected using the Wilcoxon rank-sum test implemented in Seurat, applying thresholds of adjusted $p < 0.05$ and a minimum absolute log-fold change. Analyses compared defined cell clusters as well as tumor tissue against matched normal adjacent samples. Functional enrichment was

carried out with clusterProfiler, encompassing Gene Ontology (GO) terms, KEGG pathways, and gene set enrichment analysis (GSEA). Pathway-level activity scores were derived via GSVA at either the cluster or sample level. Enriched terms achieving adjusted $p < 0.05$ were deemed significant.

Cell trajectory inference

Pseudotemporal ordering of selected cellular subpopulations was performed using Monocle 2. Cells were projected into reduced-dimensional space with DDRTree to reconstruct lineage trajectories. Key branching events were identified to highlight points of fate divergence. Genes exhibiting significant expression dynamics along pseudotime were extracted to uncover regulators driving transitional states.

Inference of copy number alterations and cellular stemness

Large-scale copy number variations (CNVs) in epithelial compartments were predicted independently using CopyKAT and SCEVAN. Cellular stemness was quantified with CytoTRACE scores. Integration of CNV patterns and stemness metrics enabled separation of malignant epithelial cells from their non-malignant counterparts.

Regulatory network reconstruction in macrophages

Transcription factor regulons within macrophage subpopulations were inferred through the SCENIC pipeline. Co-expression networks were built using GENIE3, followed by motif enrichment validation against the cisTarget database.

Intercellular signaling analysis

Ligand–receptor interactions between annotated cell populations were predicted using CommPath. Major communication pathways were illustrated through circos diagrams and dot plots for intuitive visualization.

Animal studies and bone marrow-derived macrophage preparation

All procedures involving animals received approval from the Ethics Committee of Shengjing Hospital, China Medical University, and adhered to national guidelines from the Ministry of Health of China (Document No. 55, 2001) as well as the NIH Guide for the Care and Use of Laboratory Animals (NIH Publication No. 85–23, revised 1996). C57BL/6 mice aged 6–8 weeks were maintained under controlled housing conditions (12-hour light/dark cycle with unrestricted access to food and water).

Bone marrow-derived macrophages (BMDMs) were generated by euthanizing mice via CO_2 inhalation, dissecting femurs and tibias, flushing marrow cavities, and differentiating isolated cells in DMEM medium containing 10% fetal bovine serum, 1% penicillin–streptomycin, and 10 ng/mL M-CSF (PeproTech) over 7 days. Mature adherent macrophages were harvested for subsequent experiments.

Classical (M1) activation was achieved by stimulating BMDMs ($0.5–0.7 \times 10^6$ cells/well in 12-well plates) with 10 ng/mL LPS (InvivoGen). Alternative (M2) activation was induced by 20 ng/mL IL-4 (PeproTech) treatment for 24 hours. Knockdown of STAB1 was accomplished using a commercial mouse-specific siRNA (Stabilin-1 siRNA, Santa Cruz).

Creation of tumor-influenced macrophages (TEMs)

Apoptotic bodies were prepared by treating colorectal cancer cell lines with short-wave ultraviolet light (254 nm) for 15 minutes, then allowing recovery in routine growth medium (DMEM at 37 °C with 5% CO_2) for 2–3 hours. This method routinely achieved over 80% Annexin V positivity among treated cells. The resulting conditioned supernatant from this recovery phase was collected and termed tumor-conditioned medium (TCM). Freshly prepared BMDMs were seeded into these cultures and permitted to engulf apoptotic targets over a 45-minute period. Residual unphagocytosed material was rigorously eliminated via three consecutive vigorous PBS rinses. Parallel control cultures of BMDMs received no apoptotic cell challenge but were processed through identical rinsing steps to ensure comparability.

RNA isolation and quantitative real-time PCR analysis

Cellular RNA was harvested employing TRIzol Reagent (Thermo Fisher Scientific) as per the provided guidelines. Sample concentration and integrity were evaluated on a NanoDrop device (Thermo Scientific), with progression restricted to those displaying an A260/A280 ratio of 1.9 or higher.

First-strand cDNA was generated utilizing PrimeScript™ RT Master Mix (Takara, product code RR036A) in a SimpliAmp thermocycler (Thermo Fisher) through a 15-minute reaction at 37 °C, terminated by a brief 5-second hold at 85 °C. Target amplification was executed on the QuantStudio platform (Applied

Biosystems) with iTaq™ Universal SYBR® Green Supermix (Bio-Rad, catalog #1725120). The amplification profile featured an initial 3-minute denaturation at 95 °C, succeeded by 40 cycles of 10 seconds at 95 °C, 30 seconds at 59 °C, and 30 seconds at 72 °C. Transcript abundance was normalized and expressed as fold differences calculated by the $2^{-\Delta\Delta}$Ct approach. The sequences of employed primers are presented below:

Table 1

Category / Gene	Forward Primer Sequence	Reverse Primer Sequence
Arg1	ACATTGGCTTGCG AGACGTA	ATCGGCCTTTTC TTCCTTCCC
Actb	TGACGTTGACATC CGTAAAG	GAGGAGCAATG ATCTTGATCT
Mrc1	CTCTGTTCAGCTA TTGGACGC	CGGAATTTCTGG GATTCAGCTTC
Stab1	GGCAGACGGTAC GGTCTAAAC	AGCGGCAGTCCA GAAGTATCT

Western blot analysis

Protein lysates were prepared from bone marrow-derived macrophages (BMDMs), and protein concentrations were quantified using the BCA protein assay. Equivalent protein quantities (30 µg per sample) were heated to 100 °C for denaturation, resolved by sodium dodecyl sulfate-polyacrylamide gel electrophoresis (SDS-PAGE) on 8% or 10% gels, and subsequently transferred onto polyvinylidene difluoride (PVDF) membranes (Millipore). Membranes were blocked with 5% non-fat dry milk and probed with primary antibodies overnight at 4 °C, followed by incubation with horseradish peroxidase (HRP)-conjugated secondary antibodies. Protein bands were visualized using enhanced chemiluminescence (ECL) detection reagent (Bio-Rad).

The primary antibodies employed were:

- STAB1 (1:1000 dilution, catalog # ABIN7075722, antibodies-online)
- ARG1 (1:1000 dilution, catalog # sc-47715, Santa Cruz Biotechnology)
- CD206 (1:1000 dilution, catalog # sc-58986, Santa Cruz Biotechnology)
- LRP1 (1:10,000 dilution, catalog # ab92544, Abcam)
- MERTK (1:10,000 dilution, catalog # ab95925, Abcam)
- TIM-3 (1:1000 dilution, catalog # A2516, ABclonal)
- Phospho-S6 (1:1000 dilution, catalog # sc-293144, Santa Cruz Biotechnology)
- Total S6 (1:1000 dilution, catalog # sc-74459, Santa Cruz Biotechnology)
- Phospho-4E-BP1 (1:1000 dilution, catalog # sc-293124, Santa Cruz Biotechnology)
- Total 4E-BP1 (1:1000 dilution, catalog # sc-81149, Santa Cruz Biotechnology)
- GAPDH (1:100,000 dilution, catalog # A19056, ABclonal)
- β-Actin (1:100,000 dilution, catalog # AC026, ABclonal)

The secondary antibodies used were:

- HRP-conjugated anti-mouse IgG (1:10,000 dilution, catalog # SA00001-1, Proteintech)
- HRP-conjugated anti-rabbit IgG (1:10,000 dilution, catalog # SA00001-2, Proteintech)

Statistical analysis

Results are expressed as mean ± standard error of the mean (SEM), unless specified otherwise. Primary statistical testing was conducted using GraphPad Prism version 9, with supplementary analyses performed in R and Python. Data distribution was evaluated for normality using the Shapiro–Wilk test and for equality of variances using Levene's test. Comparisons between two groups were carried out with two-sided unpaired Student's t-tests (applying Welch's correction in cases of unequal variances) or Mann–Whitney U tests for non-parametric data; paired data were analyzed using paired t-tests or Wilcoxon matched-pairs signed-rank tests. For experiments involving multiple groups, one-way or two-way analysis of variance (ANOVA) was performed, followed by Tukey's honestly significant difference (HSD) post-hoc test, with adjusted p-values reported in the figures. Pairwise comparisons within subpopulations were assessed using two-sided Wilcoxon rank-sum tests, and multiple testing correction was applied via the Benjamini–Hochberg procedure to control the false discovery rate (FDR; significance threshold $q < 0.05$), with reported q-values.

Results and Discussion

Pathology slide selection and feature analysis from COAD WSIs

This study initially included whole-slide images (WSIs) from 387 TCGA-COAD patients who also had bulk

RNA-seq and clinical data. During quality control, we removed duplicate files, non-tumor control slides, and any images with poor quality issues such as contamination, discoloration, or overlapping tissue. Following these exclusions, diagnostic tumor WSIs from 297 patients were kept for further analysis **(Figure 1a).**

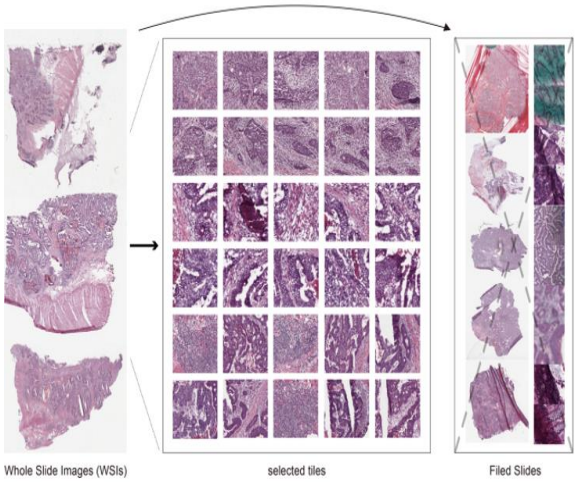

a)

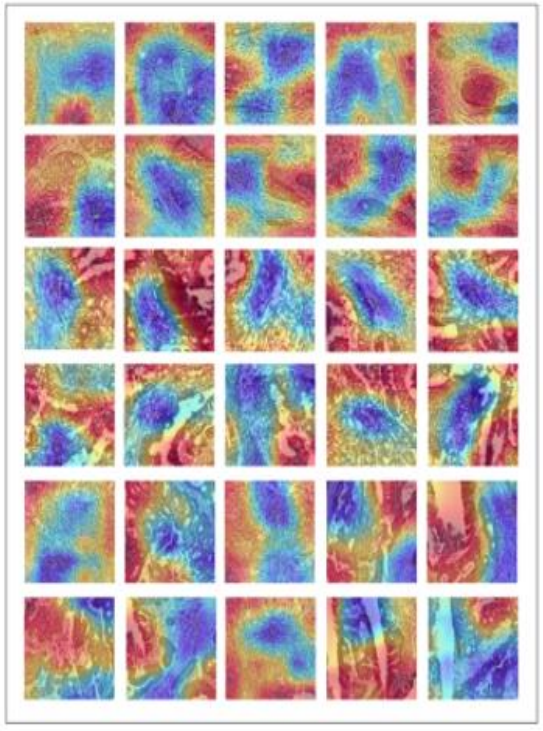

b)

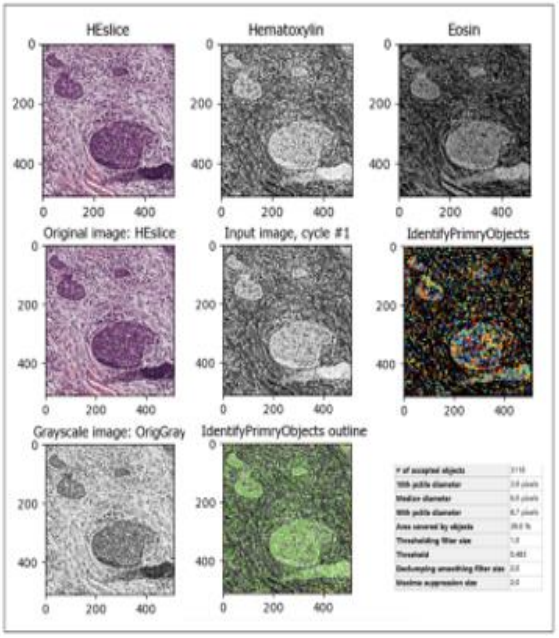

c)

Figure 1. Processing and feature extraction from whole-slide images in colorectal adenocarcinoma (COAD). (a), Selection criteria for the WSI dataset, including tile division and prioritization of informative areas. (b), Overlay of Grad-CAM activation maps on sample patches to show areas emphasized by convolutional neural networks. (c), Example pipeline for conventional morphometric analysis using CellProfiler.

High-quality regions were selected for training by loading WSIs with OpenSlide (v3.4.1) and detecting tissue areas via Histolab (v0.7.0) to mask out background and artifacts like pen marks. Ten non-overlapping patches were sampled from every WSI. Patches failing thresholds—less than 60% tissue or more than 20% artifacts—were discarded, with a minimum of five valid patches required per slide. A collaborative review by two physicians and two pathologists led to the removal of an additional 292 suboptimal patches affected by issues like air bubbles, out-of-focus areas, annotations, folds, or empty space. This process yielded 2,678 curated patches, forming a reliable digital pathology collection for subsequent feature engineering and modeling.

Histopathology images convey details at various resolutions, from overall tissue organization to subtle cellular patterns and textures. A hybrid pipeline was designed to harness both scales by merging deep neural network embeddings with hand-crafted quantitative

metrics, creating parallel streams that deliver mutually enriching representations for a rich multimodal feature space.

Deep embeddings were generated for each patch via a pretrained ResNet50 model [31], producing 2048-dimensional vectors. These were pooled at the slide level through simple averaging. For better transparency [10], Grad-CAM visualizations were created to illustrate the model's attention on clinically relevant structures **(Figure 1b).** Simultaneously, traditional metrics were derived with CellProfiler (v4.2.4) [32] after initial steps of stain separation (UnmixColors) and grayscale transformation (ColorToGray). Computed attributes included whole-patch measures (quality, overlap, texture, granulation) and segmented object properties (nuclear detection, staining intensity, shape, texture). Statistics such as mean, median, and variance were calculated across patches, resulting in 773 conventional features **(Figure 1c).**

Overall, deep embeddings from ResNet50 and quantitative metrics from CellProfiler were fused across the 2,678 curated patches to build an extensive histopathology feature repository for later survival prediction tasks.

Development of a survival prediction model using image features linked to efferocytosis

To investigate the predictive power of efferocytosis-related histopathology features in COAD, an individual efferocytosis activity index was first calculated per patient through single-sample gene set enrichment analysis (ssGSEA), based on an established panel of 137 relevant genes. In parallel, patch-level features from both ResNet50 and CellProfiler were merged into a unified multimodal feature table.

The cohort was randomly partitioned into training and validation subsets at an 80:20 split. In the training subset, Spearman correlations identified image features consistently related to efferocytosis scores ($p < 0.05$). These were further narrowed via Elastic Net regularization ($\alpha = 0.2$), retaining 78 features tied to efferocytosis **(Figure 2a).** Univariate Cox proportional hazards modeling then screened for associations with overall survival, selecting 12 key predictors to build the final risk model **(Figure 2b).**

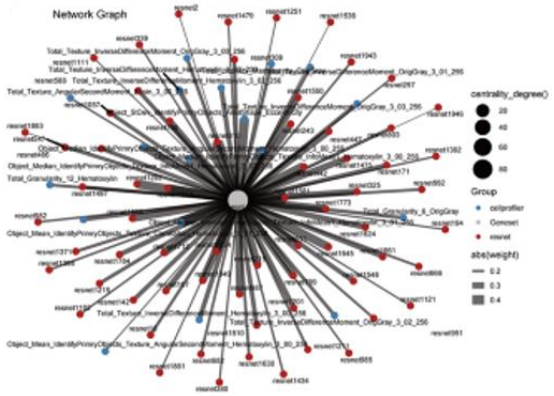

a)

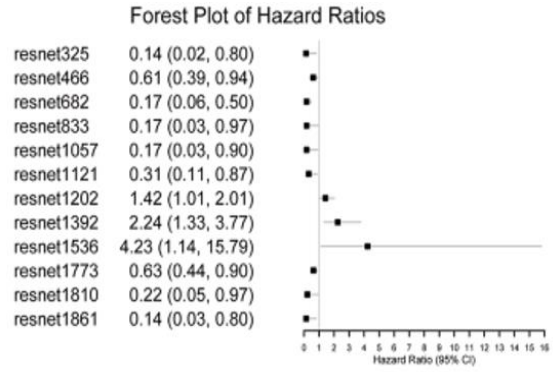

b)

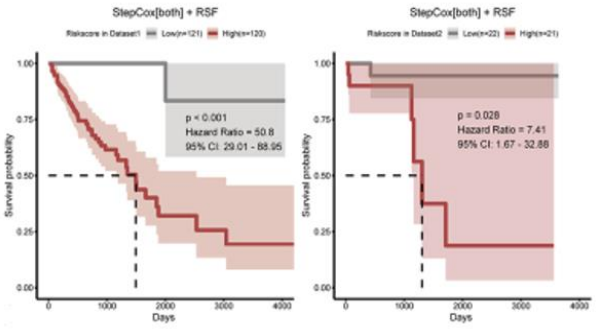

d)

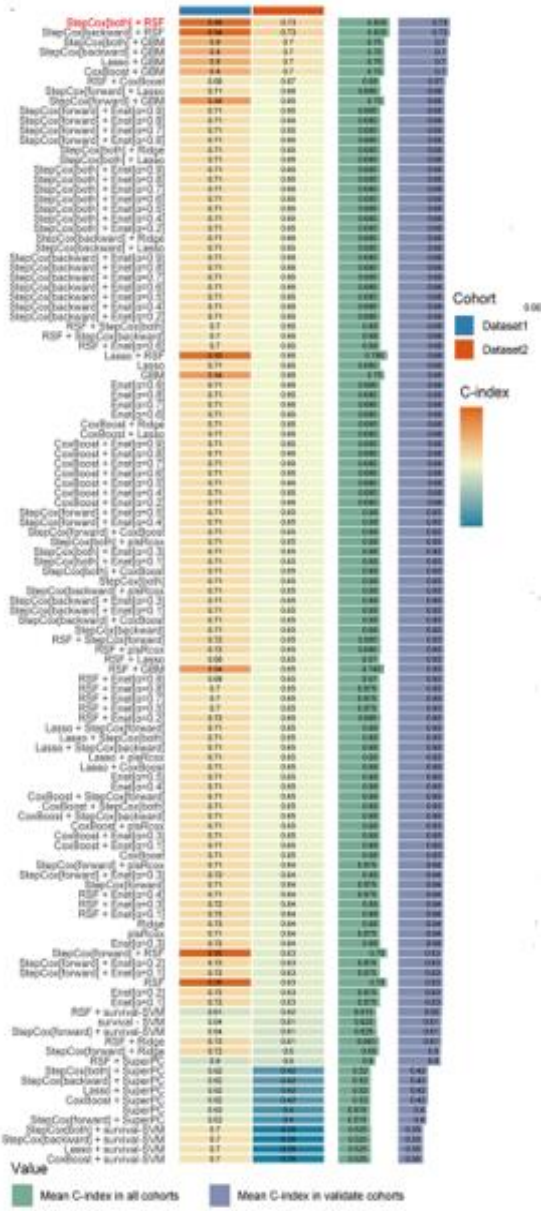

c)

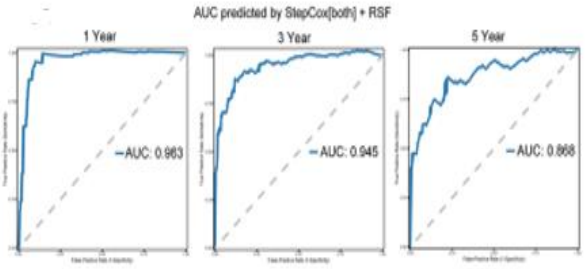

e)

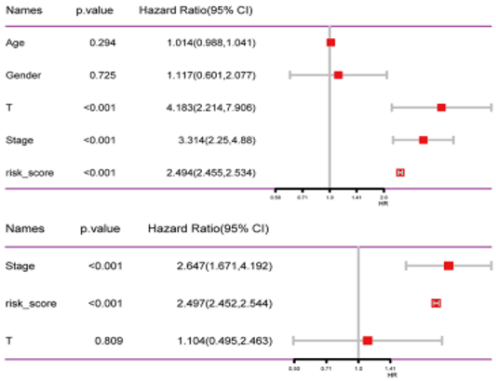

f)

Figure 2. demonstrates the development of a predictive risk scoring system founded on histopathological characteristics tied to efferocytosis. (a) Network visualization highlighting 78 histopathological traits with notable links to functional pathways involved in efferocytosis ($p < 0.05$). (b) Forest plot indicating hazard ratios for 12 histopathological traits that exhibited strong correlations with overall survival (OS). (c) One hundred distinct forecasting models were generated, and the concordance index (C-index) was determined for each across the training and validation sets. (d) Kaplan–Meier plots depicting overall survival (OS) for the StepCox $^{+}$ RSF approach in both training and validation groups. (e) Receiver operating characteristic (ROC) plots together with area under the curve (AUC) metrics for the StepCox + RSF approach in the training group. (f) Forest plot presenting hazard ratios (HRs) and 95% confidence intervals (CIs) derived from univariate and multivariate Cox proportional hazards regression.

An ensemble prognostic framework was built by integrating outputs from 100 diverse algorithmic pairings **(Figure 2c).** These pairings encompassed five primary categories of survival modeling techniques: decision tree methods (RSF, GBM), regularized Cox regressions (Elastic Net, Lasso, Ridge), forward/backward stepwise Cox selection (StepCox), gradient boosting variants (CoxBoost), and approaches involving dimensionality reduction or support vector machines (Cox-PLS, SuperPC, survival-SVM). For every model, Harrell's concordance index (C-index) was evaluated in the training and validation datasets. The StepCox combined with RSF emerged with the superior mean C-index and was designated as the top model. Survival analysis via Kaplan–Meier curves revealed that individuals assigned to the high-risk category had substantially poorer overall survival than those in the low-risk category ($p < 0.05$, **Figure 2d**). Further validation through ROC analysis underscored the model's excellent discriminatory power for survival at 1, 3, and 5 years, achieving AUC values consistently above 0.868 **(Figure 2e).**

To assess if the derived risk score contributes unique predictive value independent of routine clinical parameters, it was analyzed alongside TNM staging, patient age, and gender using both univariate and multivariate Cox regressions. Univariate results identified significant prognostic links for the risk score as well as T and N stages (all $p < 0.05$). Even after adjustment, the risk score persisted as a robust independent predictor in multivariate testing (hazard ratio [HR] = 2.497, 95% confidence interval [CI]: 2.452–2.544, $p < 0.001$) **(Figure 2f),** highlighting its prospective value in patient management.

Remarkably, this histopathology-driven model delivers predictive strength on par with the conventional TNM classification. Yet, in contrast to TNM—which demands considerable expert input and subjective evaluation—our system is entirely automated, computationally efficient, and highly consistent across applications. Such qualities render it an effective supplementary resource for swift, impartial, and uniform risk stratification, thereby supporting individualized therapeutic decisions in colon adenocarcinoma.

Multi-omics integration uncovers tumor-promoting functions of STAB1 and TREM2 in COAD

Histopathological patterns visible in tissue sections that influence clinical outcomes typically correspond to specific molecular signatures [33, 34]. To elucidate the biological processes underlying the prominent image-based traits we detected—and to pinpoint candidate drug targets connected to efferocytosis—we merged these computationally extracted features with gene expression profiles from individuals with COAD. Associations between the visual traits and transcript levels were quantified via Spearman rank correlation, leading to the assembly of an integrated trait–gene interaction network **(Figure 3a).**

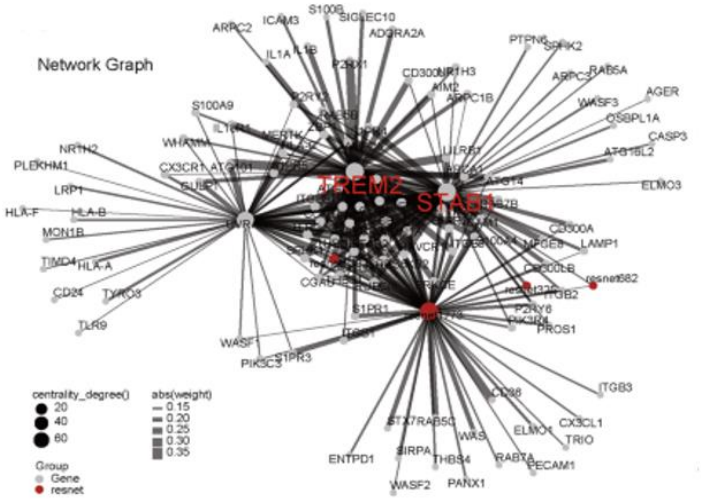

a)

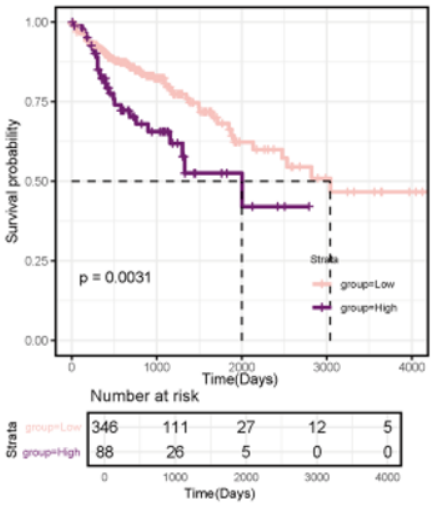
Survival probability
1.00
0.75
0.50
0.25
0.00
p = 0.0031
Strata
group=Low
group=High
0
1000
2000
3000
4000
Time(Days)
Number at risk
Strata
group=Low
group=High
346 111 27 12 5
88 26 5 0 0
0
1000
2000
3000
4000
Time(Days)

b)

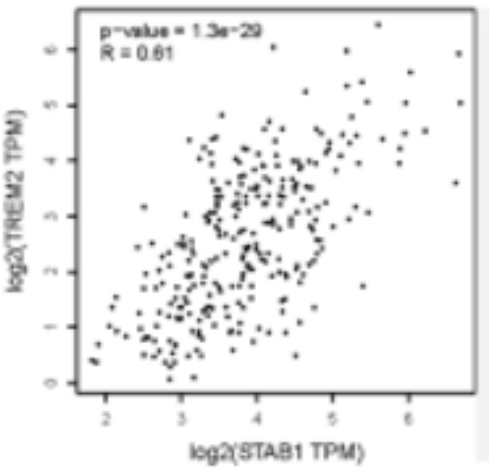
p-value = 1.3e-29
R = 0.61
log2(TREM2 TPM)
log2(STAB1 TPM)

c)

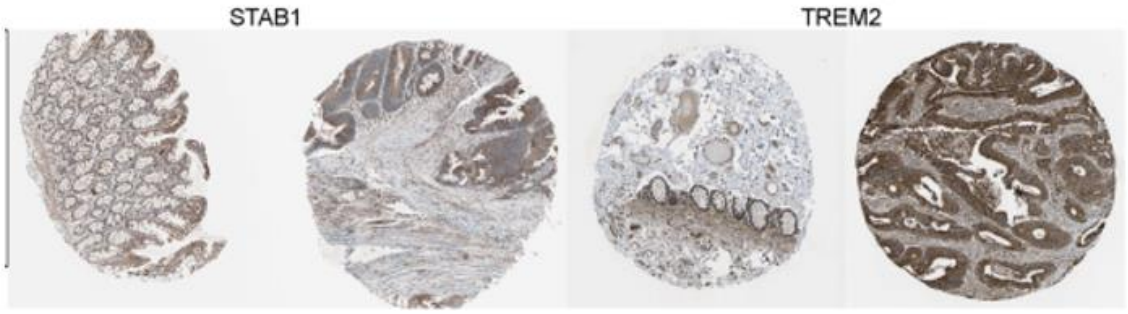
STAB1
TREM2

d)

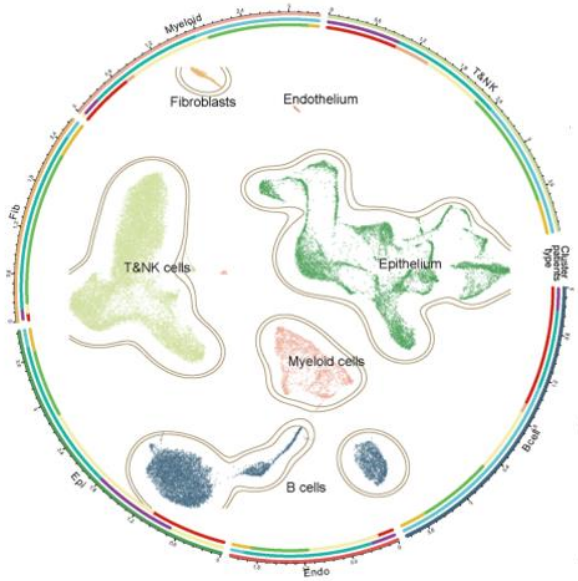
Myeloid
T&NK
Fibroblasts
Endothelium
Fib
T&NK cells
Epithelium
Myeloid cells
B cells
Epi
Endo
B cell

e)

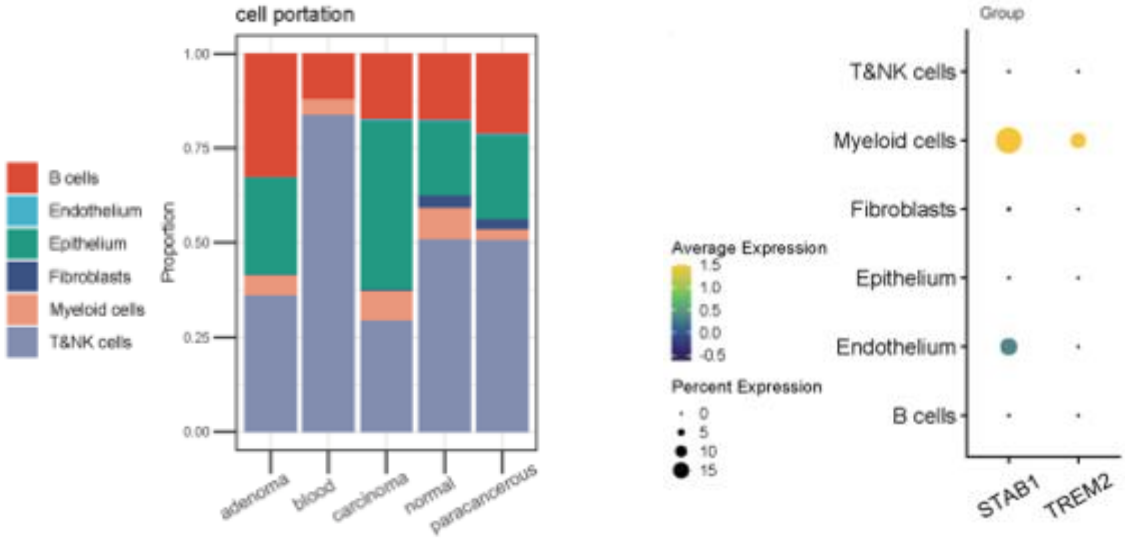

f) **g)**

Figure 3. Showcases the integration of multi-omics data to uncover the tumor-promoting functions of STAB1 and TREM2 in colon adenocarcinoma (COAD). (a) Network visualization depicting significant correlations ($p < 0.05$) between the prognostic model's key pathological features and genes involved in efferocytosis. (b) Kaplan–Meier survival plots demonstrating differences in overall survival (OS) between groups with high versus low expression of STAB1 and TREM2. (c) Analysis of bulk RNA-seq data through GEPIA2 revealing a robust positive correlation between STAB1 and TREM2 expression levels in COAD. (d) Immunohistochemistry images sourced from the Human Protein Atlas (HPA) verifying higher protein levels of STAB1 and TREM2 in COAD samples relative to normal colon tissue. The left side displays STAB1 staining in normal and tumor specimens; the right side shows TREM2. (e) UMAP visualization of single-cell RNA-seq data distinguishing six primary cell populations in COAD and surrounding tissues. (f) Bar plot illustrating the cellular composition and proportional distribution of each cell type across samples. (g) Bubble plot indicating the expression patterns of STAB1 and TREM2 in various cell types.

Findings indicated that multiple critical histopathological traits displayed strong positive associations with the immunomodulatory proteins STAB1 and TREM2, implying that these proteins might be pivotal in mediating tissue architectural alterations linked to efferocytosis. Survival analysis using Kaplan–Meier methods substantiated that elevated expression of STAB1 and TREM2 was strongly linked to unfavorable outcomes ($p < 0.05$), as individuals with high expression experienced considerably reduced median overall survival times **(Figure 3b).**

Examination of bulk RNA sequencing data demonstrated significant overexpression of both STAB1 and TREM2 in cancerous colon tissues, along with a marked positive intercorrelation **(Figure 3c).** Additionally, protein-level evidence from immunohistochemical assays in the Human Protein Atlas (HPA) database corroborated their increased abundance in COAD specimens **(Figure 3d).**

To pinpoint the specific cells expressing STAB1 and TREM2 and characterize their distribution, single-cell RNA sequencing (scRNA-seq) was conducted on primary tumors, matched adjacent non-cancerous tissues, adenomas, peripheral blood, and healthy colon samples from 13 patients with COAD. Following rigorous quality filtering and clustering, 40,949 cells were retained for analysis. These were categorized into six main populations: T/NK cells, myeloid cells, fibroblasts, epithelial cells, endothelial cells, and B cells **(Figures 3e).**

Cell type proportions varied substantially depending on tissue origin. Tumor samples were dominated by epithelial cells, while T/NK cells were the scarcest. Fibroblasts predominated in normal and paracancerous specimens but were notably reduced in tumors. Myeloid cells appeared in all sample types, yet their relative abundance was markedly elevated in malignant tissues

compared to adjacent non-tumor areas and adenomas, hinting at possible recruitment or local expansion **(Figure 3f).**

At the single-cell level, both STAB1 and TREM2 showed preferential upregulation in tumor samples and were primarily detected within myeloid lineages, exhibiting substantially greater expression compared to T cells, fibroblasts, or epithelial cells **(Figure 3g).**

Efferocytosis-mediated upregulation of STAB1 promotes M2-like polarization in tumor-associated macrophages (TAMs)

To identify the precise myeloid subset responsible for STAB1 expression, additional dimensionality reduction and subclustering were applied to the myeloid population from the single-cell dataset. Using established marker gene signatures, myeloid cells were subdivided into five categories: monocytes, conventional macrophages, tumor-associated macrophages (TAMs), dendritic cells (DCs), and neutrophils **(Figures 4a)**. Peripheral blood myeloid cells consisted mainly of monocytes, DCs, and neutrophils. Normal tissues and adjacent non-tumor regions featured a greater fraction of mature conventional macrophages with comparable profiles. In sharp contrast, tumor tissues displayed a pronounced expansion of TAMs and neutrophils, underscoring their specialized contributions to the tumor ecosystem. Adenoma samples presented a transitional composition bridging normal and fully malignant states **(Figure 4d).**

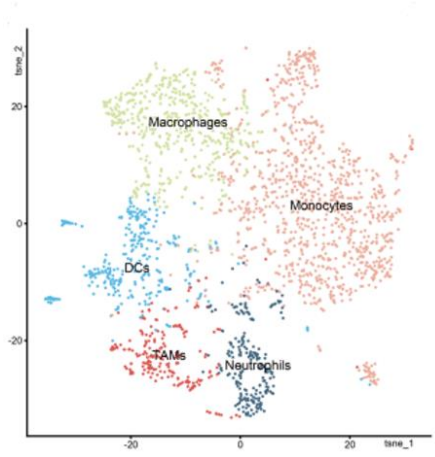

a)

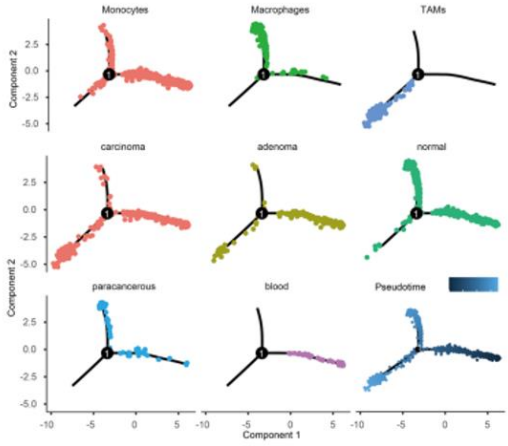

b)

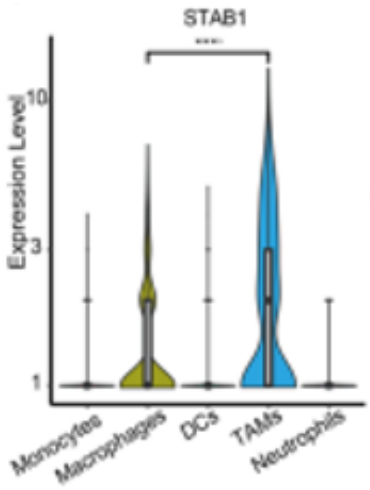

c)

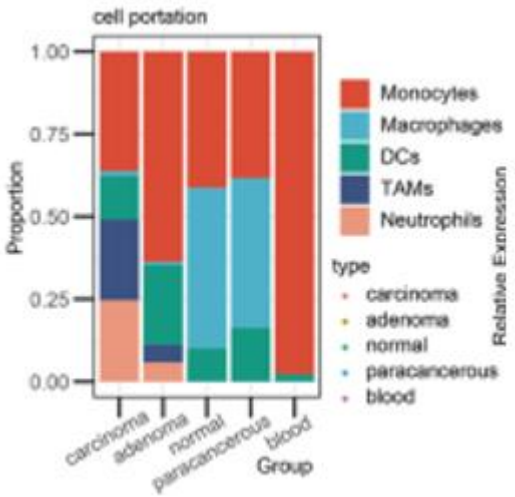

d)

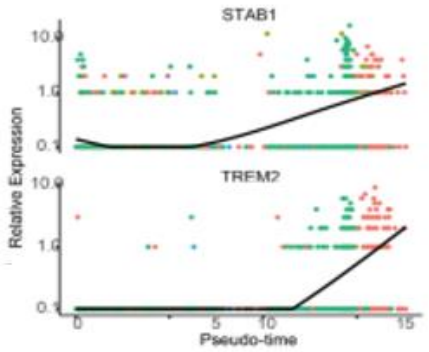
STAB1
TREM2
Relative Expression
Pseudo-time

e)

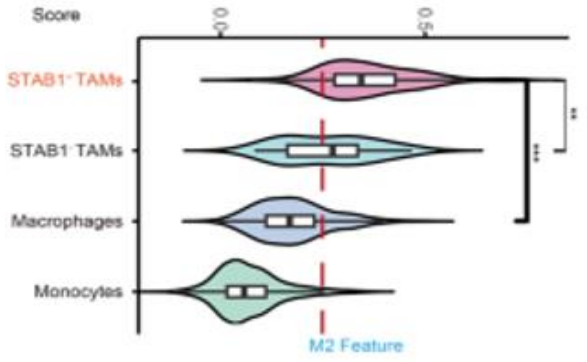
Score
STAB1+ TAMs
STAB1- TAMs
Macrophages
Monocytes
M2 Feature

f)

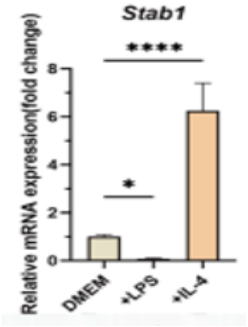
Stab1
Relative mRNA expression(fold change)
DMEM
+LPS
+IL-4

g)

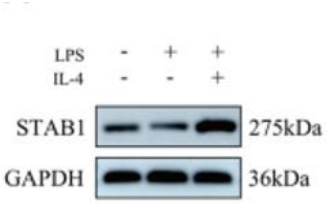
LPS
IL-4
STAB1
GAPDH
275kDa
36kDa

h)

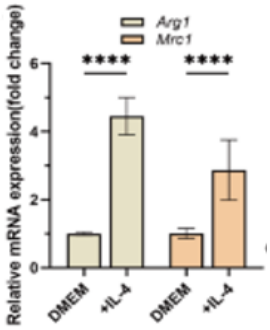
Arg1
Mrc1
Relative mRNA expression(fold change)
DMEM
+IL-4

i)

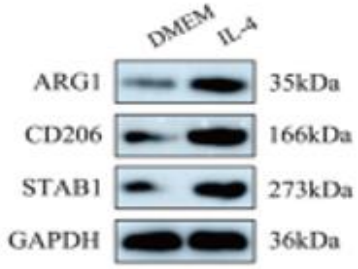
DMEM
IL-4
ARG1
CD206
STAB1
GAPDH
35kDa
166kDa
273kDa
36kDa

j)

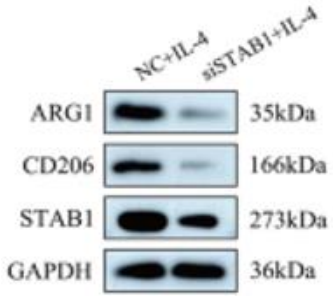
NC+IL-4
siSTAB1+IL-4
ARG1
CD206
STAB1
GAPDH
35kDa
166kDa
273kDa
36kDa

k)

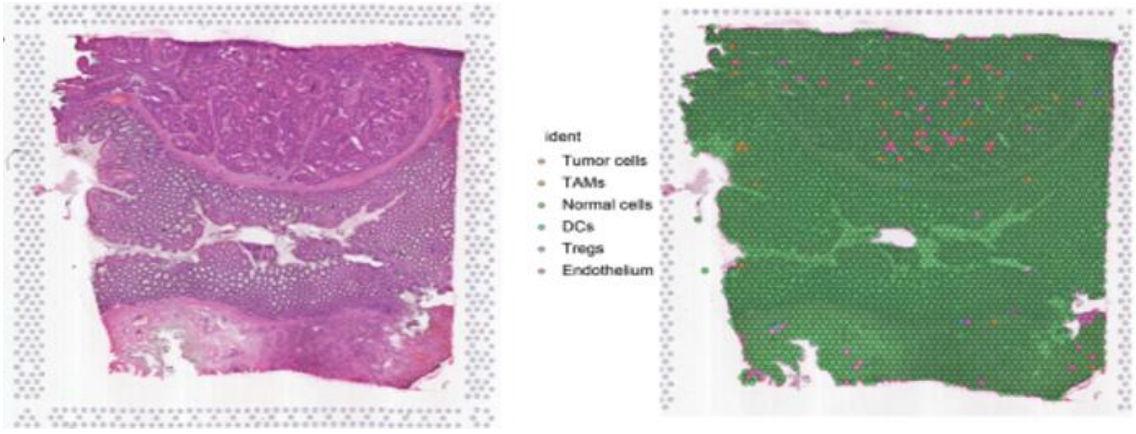
ident
Tumor cells
TAMs
Normal cells
DCs
Tregs
Endothelium

l)

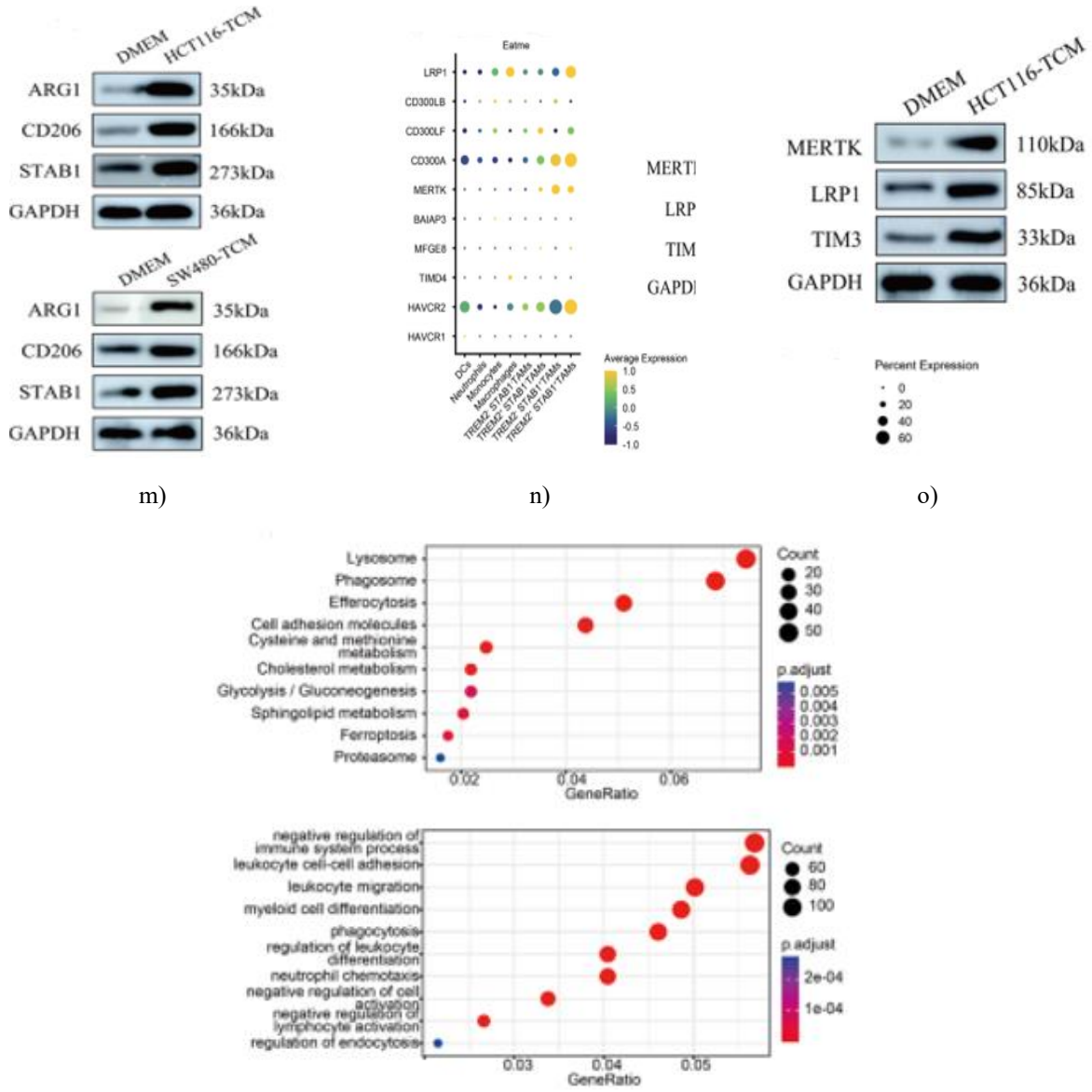

Figure 4. Elucidates how efferocytosis-triggered elevation of STAB1 promotes M2-like polarization in tumor-associated macrophages (TAMs). (a) t-SNE visualization of myeloid subpopulations, with clusters distinguished by color. (b) Pseudotime trajectory constructed using Monocle 2, displaying annotated cell types and their respective tissue sources. (c) Violin plot depicting the distribution of STAB1 expression across various sample categories. (d) Bar chart representing the relative proportions and makeup of each myeloid subtype in different samples. (e) Scatter plot illustrating changes in STAB1 expression across pseudotime, accompanied by a fitted trendline (black) highlighting dynamic regulation. (f) Violin plots contrasting M2-polarization scores among TAM subsets. Comparisons performed using pairwise two-sided Wilcoxon tests adjusted with Benjamini–Hochberg FDR; q-values indicated. Significance levels: ***$q < 0.001$, **$q < 0.01$. (g) qPCR results quantifying STAB1 mRNA levels in wild-type (WT) murine bone marrow-derived macrophages (BMDMs) exposed to DMEM (control), IL-4 (20 ng/mL), or LPS (100 ng/mL). (h) Western blot showing STAB1 protein expression aligned with the qPCR data in (g). (i) qPCR measurement of established M2 macrophage markers in WT and IL-4-treated BMDMs. (j) Western blot evaluating M2 markers and STAB1 protein in WT versus IL-4-stimulated BMDMs. (k) Western blot assessing M2 markers and STAB1 after siRNA-based knockdown of STAB1 in IL-4-

treated BMDMs. (l) H&E-stained sections of COAD tissues with overlaid spatial transcriptomic (ST) clusters annotated by corresponding cell type identities. (m) Western blot examining STAB1 and M2 marker expression in WT BMDMs grown in complete media versus tumor-conditioned media with added apoptotic colon cancer cells. (n) Bubble plot illustrating expression of "eat-me" signal receptors in different cell populations. (o) Western blot comparing "eat-me" signal receptor levels in WT BMDMs under standard or conditioned media, both with apoptotic tumor cell supplementation. (p) Gene Ontology (GO) Biological Process terms and KEGG pathways enriched in genes overexpressed in STAB1+ TAMs.

Trajectory inference using pseudotime revealed that myeloid differentiation initiates from monocytes and diverges into two separate lineages culminating in conventional macrophages and TAMs, respectively, thereby confirming the robustness of the subclustering **(Figures 4b).** Since TREM2 is a well-established marker selectively abundant in TAMs [35], we closely inspected STAB1 distribution. STAB1 was also predominantly enriched in TAMs, showing clear statistical separation from other myeloid subsets **(Figure 4c).** Throughout the reconstructed developmental trajectory, both STAB1 and TREM2 displayed peak expression in later phases, with STAB1 activation occurring earlier than TREM2 **(Figure 4e).** This temporal pattern implies that STAB1 could contribute to the initial stages of TAM maturation.

Tumor-associated macrophages commonly acquire an immunosuppressive M2-like state [36]. Accordingly, we divided TAMs into $STAB1^{+}$ and STAB1− groups and computed M2 polarization scores across the monocyte-to-macrophage continuum. $STAB1^{+}$ TAMs consistently showed markedly elevated M2 scores relative to STAB1− TAMs **(Figure 4f),** indicating that STAB1 likely functions as an important driver of immunosuppressive polarization in TAMs.

To probe this relationship experimentally, we performed in vitro studies on macrophage polarization and STAB1 involvement. Bone marrow-derived macrophages (BMDMs) were treated for 24 hours with either IL-4 or lipopolysaccharide (LPS) to induce M2 or M1 phenotypes, respectively. IL-4 stimulation strongly increased both STAB1 mRNA and protein levels in M2 macrophages, while LPS-treated M1 cells showed no change in STAB1 **(Figure 4g and 4h).** Importantly, STAB1 knockdown via siRNA substantially reduced IL-4-driven upregulation of classic M2 markers Arg1 and CD206 **(Figures 4I–K)**. These results establish that STAB1 is required for IL-4-mediated M2 immunosuppressive differentiation but not for LPS-induced proinflammatory M1 activation.

Previous work indicates that TAMs in the tumor microenvironment perform efferocytosis of apoptotic cancer cells, which suppresses antigen release/presentation and simultaneously shifts macrophages toward a protumor M2 state. To corroborate this in COAD, we mapped scRNA-seq-derived immune cell annotations onto spatial transcriptomic data. Malignant epithelial cells and TAMs were prominently co-localized in tumor regions, suggesting close physical interactions **(Figures 4l).** To mimic tumor-educated macrophages in vitro, we exposed M-CSF-differentiated BMDMs to apoptotic colorectal cancer cells using published methods [37, 38]. Residual non-phagocytosed apoptotic cells were rigorously removed by repeated PBS washing, and parallel sham controls (no apoptotic cells) underwent identical processing (see Methods). This exposure markedly boosted protein levels of STAB1, Arg1, and CD206 in tumor-educated macrophages **(Figures 4m),** an effect not seen in standard culture conditions.

We next characterized the functional profile of $STAB1^{+}$ TAMs in greater detail. Transcriptome analysis showed strong upregulation of multiple "eat-me" receptors such as MERTK, AXL, and TIMD4 [39] in this subset **(Figure. 4n)**. Western blotting validated enhanced "eat-me" signaling in tumor-educated macrophages **(Figure 4o).** Enrichment analysis of GO Biological Processes and KEGG pathways identified significant overrepresentation of terms linked to efferocytosis, phagocytosis, cell adhesion/migration, metabolic shifts, and immunosuppression **(Figure 4p).** In line with observations in ovarian cancer, STAB1 facilitates macrophage uptake and degradation of apoptotic tumor cells, thereby dampening downstream antitumor immunity [40].

Taken together, these data illustrate that in the colon adenocarcinoma microenvironment, macrophage efferocytosis of apoptotic tumor cells induces STAB1 expression, which in turn fosters polarization toward a tumor-supportive M2-like TAM phenotype. This positions STAB1 as a crucial mediator of TAM specialization and tumor immune escape.

STAB1⁺ TAMs remodel the tumor microenvironment through mTORC1 activation and multicellular interactions

Gene set enrichment analysis (GSEA) demonstrated that STAB1⁺ TAMs were strongly enriched for hallmark gene sets including "hypoxia," "glycolysis," "inflammatory response," and "mTORC1 signaling" **(Figure 5a).** These enrichments point to a central involvement of STAB1⁺ TAMs in regulating cell proliferation and metabolic adaptation within the tumor.

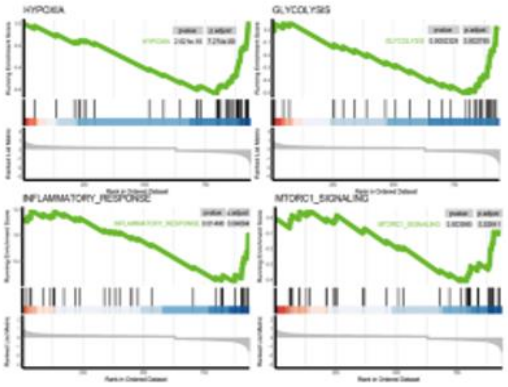

a)

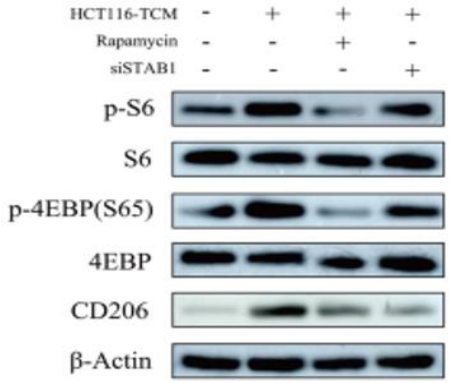

b)

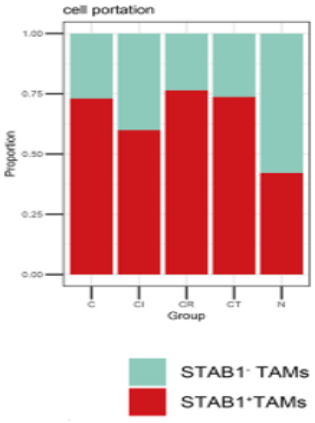

c)

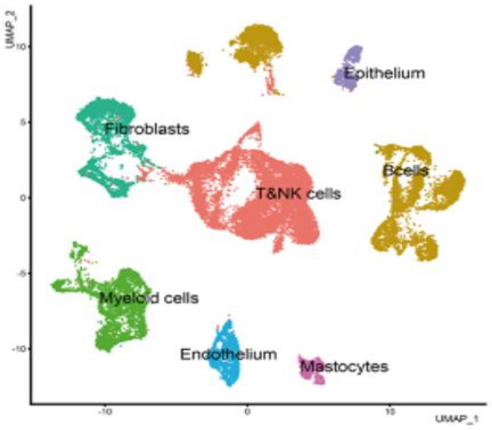

d)

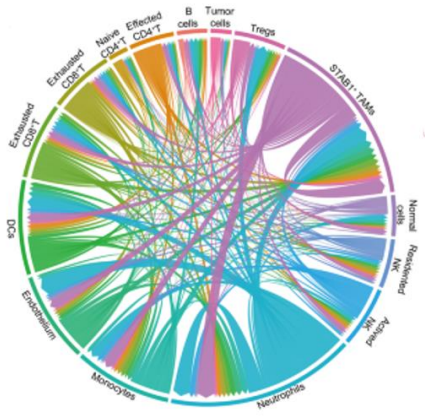

e)

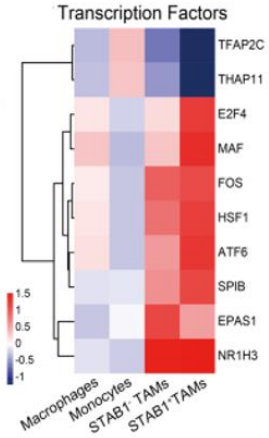

g)

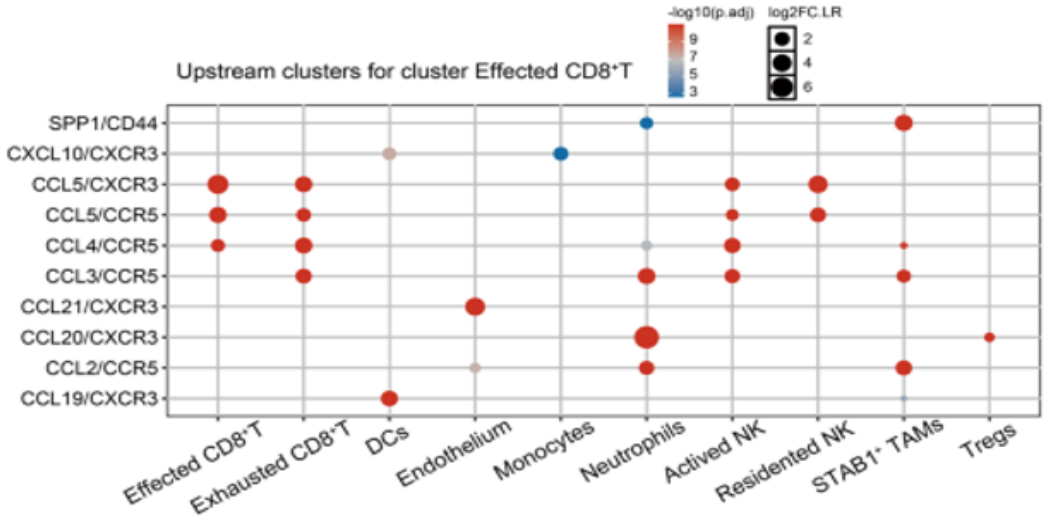

f)

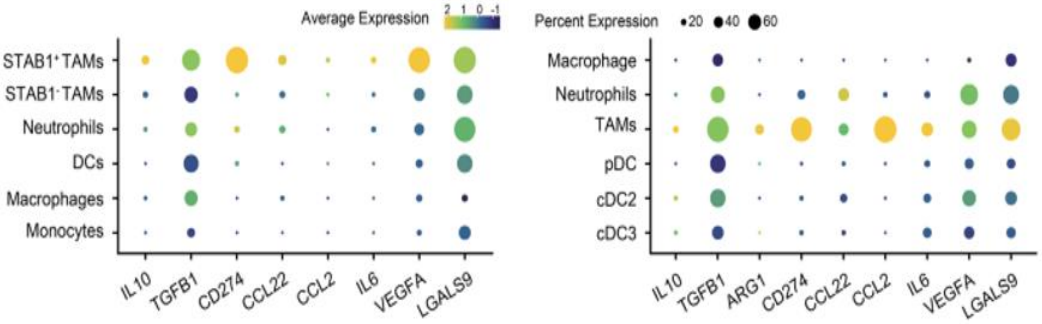

h)

Figure 5. STAB1$^+$ TAMs shape the tumor microenvironment via mTORC1 signaling and intercellular networks**.**

(a) GSEA highlighting pathways enriched in STAB1$^+$ TAMs. (b) Western blot analysis of indicated proteins in wild-type BMDMs treated with HCT116-TCM, in the presence or absence of 100 nM rapamycin or siSTAB1 for 24 hours. (c) Bar plot showing the distribution of STAB1± TAMs across different therapeutic regimens: chemotherapy alone (c), chemotherapy plus anti–PD-1 (CI), chemoradiotherapy (CR), chemotherapy plus bevacizumab (CT), and untreated controls (N). (d) UMAP of single-cell RNA-seq data identifies seven main cell populations in treated COAD and adjacent tissues. (e) CommPath networks reveal the functional diversity of TAMs. (f) CommPath analysis identifies upstream pathways modulating effector CD8$^+$ T cell activity. (g) Heatmap displaying transcription factor activity across myeloid subsets; color intensity represents regulon scores. (h) Bubble plot depicting expression of immunosuppressive factors across cell types; bubble size indicates the proportion of expressing cells, while color intensity reflects average expression levels.

To investigate STAB1's role in activating mTORC1, we measured phosphorylation of downstream effectors S6 and 4E-BP1. TEMs exposed to tumor-conditioned medium exhibited pronounced increases in p-S6 and p-4EBP1, whereas inhibiting STAB1 strongly reduced these phosphorylation levels. These results support the conclusion that STAB1 promotes an M2-like, immunosuppressive TAM phenotype through mTORC1 activation **(Figure 5b).**

We next examined STAB1 expression in COAD tumors following neoadjuvant therapy, including chemotherapy alone, chemotherapy plus anti–PD-1, chemoradiotherapy, and chemotherapy plus bevacizumab, compared to untreated tumors. Therapy consistently elevated STAB1 expression, accompanied by increased macrophage infiltration **(Figures 5c and**

5d). These observations suggest that therapy-induced tumor cell death and inflammation enhance efferocytosis, which upregulates STAB1 and drives macrophages toward an immunosuppressive state. Analysis of chemotherapy response datasets (GEO: GSE30034 and GSE16648) showed higher STAB1 levels in resistant tumors versus sensitive ones**,** implying that STAB1 may contribute to therapeutic resistance.

To explore the regulatory mechanisms and functional networks of STAB1$^+$ TAMs, we conducted transcription factor activity and intercellular communication analyses. STAB1$^+$ TAMs demonstrated increased activity of MAF and E2F4, with decreased activity of TFAP2C and THAP11 **(Figure 5g),** indicating that distinct transcriptional programs underlie their polarization. Communication analyses revealed that STAB1$^+$ TAMs act as central hubs within the TME, showing particularly strong interactions with neutrophils **(Figure 5e),** consistent with prior observations of neutrophil enrichment **(Figure 4d).** Ligand–receptor mapping highlighted complex signaling between STAB1$^+$ TAMs, neutrophils, immune cells, and tumor cells **(Figures 5f).** Reciprocal chemotactic signals involving CCL2, CCR1, and HBEGF enhance recruitment and sustain immunosuppressive phenotypes. Furthermore, STAB1$^+$ TAM-derived factors such as PD-L1 and IL-10 reinforce immune suppression, establishing a positive feedback loop that maintains a tumor-permissive environment. Upregulation of additional ligands, including SPP1, CD44, NRG1, and CCR5, promotes interactions with multiple immune populations, supporting tumor growth and metastasis.

In conclusion, STAB1$^+$ TAMs play a key role in shaping an immunosuppressive tumor microenvironment through mTORC1-mediated signaling and dynamic intercellular networks, emphasizing their central role in colon cancer progression.

In this work, we developed a prognostic model for COAD that integrates histopathology, transcriptomics, and clinical information. By extracting histological features linked to efferocytosis from HE-stained slides, we stratified patients into high- and low-risk groups for overall survival. We extended this approach by incorporating bulk RNA-seq, single-cell RNA-seq, and spatial transcriptomics to explore the immunosuppressive landscape of the tumor microenvironment. Through this integrative analysis, STAB1$^+$ TAMs emerged as key regulators of the TME, demonstrating the value of combining multi-omics data with computational modeling for precision prognosis in COAD.

Mechanistically, we identified a distinct subset of TAMs characterized by high STAB1 expression. These cells exhibited elevated efferocytosis-related markers and enhanced mTORC1 signaling, correlating with their M2-like, tumor-supportive phenotype. Previous studies have shown that macrophages with high STAB1 levels display increased efferocytosis—the clearance of apoptotic cells—while suppressing antigen presentation, thereby limiting antitumor immune responses [41, 42]. In murine models of colorectal cancer, tumor growth was largely dependent on macrophage STAB1, and therapeutic inhibition of STAB1 shifted TAMs toward a pro-inflammatory, antigen-presenting state, restoring CD8$^+$ T-cell activity and antitumor function [43]. Our findings are consistent with these observations, highlighting enhanced efferocytosis in STAB1$^+$ TAMs.

We propose that in tumors, persistent apoptosis generates “eat-me” signals that recruit macrophages to clear dying cells. This activity upregulates STAB1, further enhancing efferocytosis and driving macrophages toward an immunosuppressive M2-like phenotype. This establishes a self-reinforcing STAB1-mediated loop that promotes immune evasion and tumor progression. Notably, we observed that neoadjuvant therapy increased STAB1$^+$ TAM infiltration, likely due to therapy-induced apoptosis amplifying efferocytosis. Similar phenomena have been reported in ovarian cancer, where chemotherapy increased macrophage STAB1 expression, and combining chemotherapy with anti-STAB1 antibodies improved survival in syngeneic models [40]. These data suggest that therapeutic interventions may inadvertently strengthen immunosuppressive networks via STAB1, emphasizing the need to consider efferocytosis-driven suppression in treatment design [44].

Although TREM2$^+$ macrophages are often enriched in immunosuppressive TMEs, emerging evidence suggests that TREM2 primarily reflects metabolic reprogramming rather than directly driving immunosuppression [35, 45, 46]. In breast cancer, STAB1$^+$/TREM2high TAMs—not TREM2 expression alone—were identified as the population suppressing T-cell proliferation and enriched in ICB-resistant patients [47]. As a scavenger receptor [34, 48], STAB1 mediates efferocytosis and orchestrates transcriptional reprogramming, making it a promising therapeutic target. Accordingly, STAB1$^+$ TAMs appear as a distinct, phagocytosis-reprogrammed population.

Previous studies indicate that STAB1 inhibition can elicit antitumor effects comparable to anti–PD-1 therapy, and may enhance efficacy in combination [49, 50]. In gastric cancer, STAB1$^+$ TAMs strongly suppress T-cell proliferation and function, with high infiltration associated with poor or adaptive resistance to PD-1 blockade [51, 52]. STAB1 blockade restores CD8$^+$ T-cell activity, suggesting a dual approach in which myeloid reprogramming (STAB1) complements T-cell reinvigoration (PD-1) to enhance tumor control. Beyond gastric cancer, STAB1 levels correlate with poor neoadjuvant chemotherapy response in urothelial bladder cancer and adverse prognosis in CN-AML. The MATINS trial (NCT03733990) further supports STAB1 targeting: the humanized antibody bexmarilimab (FP-1305) was well tolerated, and pharmacodynamic analyses showed macrophage reprogramming in ~30–40% of patients with refractory or "cold" tumors [53-55]. Collectively, these findings establish STAB1 as a clinically relevant target in COAD, particularly in patients resistant to conventional immune checkpoint inhibitors.

Dual blockade of STAB1 and PD-1 is a rational therapeutic strategy for patients unresponsive to PD-1 monotherapy [56-58]. While PD-1 inhibition revives exhausted T cells, STAB1 blockade limits TAM-mediated sequestration of antigens and danger signals, improving antigen presentation and tumor immunogenicity. Together, these mechanisms are expected to enhance CD8$^+$ T-cell infiltration and cytotoxicity [49]. Our histopathology–efferocytosis model identifies patients likely to benefit from STAB1-targeted therapy [50, 59], providing a framework for guiding treatment in ICB-refractory cases.

From a translational standpoint, our pathology–efferocytosis fusion risk score achieves prognostic accuracy comparable to TNM staging, while allowing automated extraction of prognostic features from HE slides. This offers a clinically feasible method for individualized risk assessment and therapy guidance. Unlike prior multi-omics studies, our model emphasizes efferocytosis-related histopathological markers, underscoring their prognostic and therapeutic relevance.

Nonetheless, our study has limitations. First, as the model was developed using TCGA data, prospective multicenter validation is needed to ensure generalizability and reduce bias. Additional studies focusing on patients with suboptimal responses to adjuvant or neoadjuvant therapy would facilitate model refinement. Future work should also explore advanced image encoders to enhance predictive performance. Second, our in vitro assays using BMDMs confirmed that efferocytosis induces an M2-like immunosuppressive state, supporting the rationale for combining STAB1 blockade with ICIs, though potential compensatory myeloid pathways may limit efficacy. Third, in vivo validation of STAB1–mTORC1 targeting, alone or combined with ICIs, remains to be performed. Future studies should include expanded patient cohorts, humanized mouse or organoid models, preclinical testing of combination regimens, and development of STAB1-targeted therapies including antibodies or small molecules.

Conclusion

Cutting-edge imaging analysis combined with deep learning is transforming both cancer research and clinical decision-making. By linking multi-omics data with histopathological image features, we developed a prognostic framework that not only predicts patient outcomes with high accuracy but also supports tailored therapeutic strategies, highlighting its potential for clinical translation.

Notably, our results connect molecular mechanisms to tissue-level morphology, identifying STAB1$^+$ TAMs as key drivers of efferocytosis-mediated mTORC1 activation and the establishment of an immunosuppressive microenvironment in COAD. These mechanistic insights provide a strong foundation for personalized immunotherapies aimed at STAB1$^+$ TAMs, offering a promising avenue to enhance clinical outcomes in COAD patients.

Acknowledgments: None

Conflict of Interest: None

Financial Support: None

Ethics Statement: None

References

1. Siegel RL, Miller KD, Wagle NS, Jemal A. Cancer statistics, 2023. CA Cancer J Clin. 2023;73:17–48.
2. Zeng D, et al. Comparison of the efficacy of neoadjuvant chemotherapy and neoadjuvant chemoradiotherapy in locally advanced rectal cancer

patients: meta-analysis of randomized controlled trials. Int J Surg. 2025;111:2686.
3. Li Q, Lu Y, Wang D. Differential survival outcomes and prognostic factors across surgical approaches for colorectal cancer: analysis of 5000 patients from the seer database. Curr Probl Surg. 2025;70:101839.
4. Yu W, Lin Y, Huang M, Du Y, Ye Z. The connection between surgical margins in liver metastases from colorectal cancer and patient prognosis: a mini review. Curr Probl Surg. 2025;63:101700.
5. Sherafat NS, et al. Rationale of using immune checkpoint inhibitors (ICIs) and anti-angiogenic agents in cancer treatment from a molecular perspective. Clin Exp Med. 2025;25:238.
6. Cesano A, et al. Advances in the understanding and therapeutic manipulation of cancer immune responsiveness: a Society for Immunotherapy of Cancer (SITC) review. J Immunother Cancer. 2025;13:e008876.
7. Cai Q, et al. Building smart car T cell therapies: the path to overcome current challenges. Cancer Cell. 2023;41:1689–95.
8. Mao W. Overcoming current challenges to T-cell receptor therapy via metabolic targeting to increase antitumor efficacy, durability, and tolerability. Front Immunol. 2022;13:1056622.
9. Kamrani A, et al. New immunotherapy approaches for colorectal cancer: focusing on CAR-T cell, BiTE, and oncolytic viruses. Cell Commun Signal. 2024;22.
10. Transformer-based biomarker prediction from colorectal cancer histology:A large-scale multicentric study. Cancer Cell. 2023;41:1650–61.e4.
11. Chen Y, et al. Tumor-associated macrophages: an accomplice in solid tumor progression. J Biomed Sci. 2019;26(78).
12. Cancer stem cells and tumor-associated macrophages: Interactions and therapeutic opportunities. Cancer Lett. 2025;624:217737.
13. Hatthakarnkul P, et al. Molecular mechanisms of tumour budding and its association with microenvironment in colorectal cancer. Clin Sci. 2022;136:521–35.
14. Aghapour SA, et al. Investigating the dynamic interplay between cellular immunity and tumor cells in the fight against cancer: an updated comprehensive review. Iran J Blood Cancer. 2024;16:84–101.
15. Zhang H, et al. Define cancer-associated fibroblasts (CAFs) in the tumor microenvironment: new opportunities in cancer immunotherapy and advances in clinical trials. Mol Cancer. 2023;22:159.
16. Zhou L, et al. Lipid droplet efferocytosis attenuates proinflammatory signaling in macrophages via TREM2- and MS4A7-dependent mechanisms. Cell Rep. 2025;44.
17. Mechanism of adipose-derived stem cell-derived extracellular vesicles affecting macrophage efferocytosis by mediating ADAM17/MerTK in the apoptosis of tubular epithelial cells after sepsis-associated acute kidney injury. Transl Res. 2025;281:14–30.
18. Lin J, et al. MerTK-mediated efferocytosis promotes immune tolerance and tumor progression in osteosarcoma through enhancing M2 polarization and PD-L1 expression. OncoImmunology. 2022;11.
19. Stanford JC, et al. Efferocytosis produces a prometastatic landscape during postpartum mammary gland involution. J Clin Invest. 2014;124:4737–52.
20. Polarization of prostate cancer-associated macrophages is induced by milk fat globule-EGF factor 8 (MFG-E8)-mediated Efferocytosis. J Biol Chem. 2014;289:24560–72.
21. Bahreiny SS, Ahangarpour A, Rajaei E, Sharifani MS, Aghaei M. Meta-analytical and meta-regression evaluation of subclinical Hyperthyroidism's effect on male reproductive health: hormonal and seminal perspectives. Reprod Sci Thousand Oaks Calif. 2024;31:2957–71.
22. Aval OS, et al. Galectin-9: a double-edged sword in acute myeloid leukemia. Ann Hematol. 2025;104:3077–90.
23. Torabizadeh M, et al. The association of nasal and blood eosinophils with serum IgE level in allergic rhinitis and asthma: a case-control study. Health Sci Rep. 2024;7:e70191.
24. PMFN-SSL: self-supervised learning-based progressive multimodal fusion network for cancer diagnosis and prognosis. Knowl-Based Syst. 2024;289:111502.
25. Feng B, et al. Ligand-receptor interactions combined with histopathology for improved prognostic modeling in HPV-negative head and neck squamous cell carcinoma. Npj Precis Oncol. 2025;9(57).
26. Bjartell A, et al. Validation of a digital pathology-based multimodal artificial intelligence biomarker in

a prospective, real-world prostate cancer cohort treated with prostatectomy. Clin Cancer Res. 2025;31:1546–53.
27. Ganta L, Sinduja P, Priyadharshini R. Knowledge and awareness of the use of artificial intelligence in digital pathology. 2023 International Conference on Business Analytics for Technology and Security (ICBATS). 2023. pp. 1–6. https://doi.org/10.1109/ICBATS57792.2023.10111238.
28. Yu Y, et al. Artificial intelligence-based multi-modal multi-tasks analysis reveals tumor molecular heterogeneity, predicts preoperative lymph node metastasis and prognosis in papillary thyroid carcinoma: a retrospective study. Int J Surg. 2025;111:839.
29. Ding G-Y, et al. Mining the interpretable prognostic features from pathological image of intrahepatic cholangiocarcinoma using multi-modal deep learning. BMC Med. 2024;22:282.
30. A pathology-based diagnosis and prognosis intelligent system for oral squamous cell carcinoma using semi-supervised learning. Expert Syst Appl. 2024;254:124242.
31. A nested case-control study of serum polychlorinated biphenyls and papillary thyroid cancer risk among U.S. military service members. Environ Res. 2022;212:113367.
32. Carpenter AE, et al. CellProfiler: image analysis software for identifying and quantifying cell phenotypes. Genome Biol. 2006;7:R100.
33. Explainability-based graph augmentation for out-of-distribution robustness in digital pathology. Knowl-Based Syst. 2025;320:113640.
34. Gheibi Hayat SM, Bianconi V, Pirro M, Sahebkar A. Efferocytosis: molecular mechanisms and pathophysiological perspectives. Immunol Cell Biol. 2019;97:124–33.
35. Fang C, et al. TREM2 promotes macrophage polarization from M1 to M2 and suppresses osteoarthritis through the NF-κB/CXCL3 axis. Int J Biol Sci. 2024;20:1992–2007.
36. Zhao W, et al. M2-like TAMs function reversal contributes to breast cancer eradication by combination dual immune checkpoint blockade and photothermal therapy. Small. 2021;17.
37. Wang Y, et al. Mitochondrial fission promotes the continued clearance of apoptotic cells by macrophages. Cell. 2017;171:331–45.e22.
38. Cai Z, et al. Targeting PHGDH reverses the immunosuppressive phenotype of tumor-associated macrophages through α-ketoglutarate and mTORC1 signaling. Cell Mol Immunol. 2024;21:448–65.
39. Evans F, et al. CD300f immune receptor contributes to healthy aging by regulating inflammaging, metabolism, and cognitive decline. Cell Rep. 2023;42.
40. Elorbany S, et al. Immunotherapy that improves response to chemotherapy in high-grade serous ovarian cancer. Nat Commun. 2024;15:10144.
41. Lennon-Duménil A-M, et al. Analysis of protease activity in live antigen-presenting cells shows regulation of the phagosomal proteolytic contents during dendritic cell activation. J Exp Med. 2002;196:529–40.
42. Delamarre L, Pack M, Chang H, Mellman I, Trombetta ES. Differential lysosomal proteolysis in antigen-presenting cells determines antigen fate. Science. 2005;307:1630–34.
43. Viitala M, et al. Immunotherapeutic blockade of macrophage clever-1 reactivates the CD8+ T-cell response against immunosuppressive tumors. Clin Cancer researchoff J Am Assoc Cancer Res. 2019;25:3289–303.
44. Karsch-Bluman A, et al. Tissue necrosis and its role in cancer progression. Oncogene. 2019;38:1920–35.
45. Zhao X, et al. A new perspective on the therapeutic potential of tumor metastasis: targeting the metabolic interactions between TAMs and tumor cells. Int J Biol Sci. 2024;20:5109–26.
46. Binnewies M, et al. Targeting TREM2 on tumor-associated macrophages enhances immunotherapy. Cell Rep. 2021;37:109844.
47. Timperi E, et al. Lipid-associated macrophages are induced by cancer-associated fibroblasts and mediate immune suppression in breast cancer. Cancer Res. 2022;82:3291–306.
48. Yin J, Luo J, Wang L, Liu L, Liu L. STAB1 promotes acute myeloid leukemia progression by activating the IKK/NF-κB pathway and increasing M2 macrophage polarization. Cancer Sci. 2025;116:1508–21.
49. Peranzoni E, et al. Macrophages impede CD8 T cells from reaching tumor cells and limit the efficacy of anti-PD-1 treatment. Proc Natl Acad Sci U.S.A. 2018;115:E4041–50.

50. Jiang P, et al. Signatures of T cell dysfunction and exclusion predict cancer immunotherapy response. Nat Med. 2018;24:1550–58.
51. Yu K, et al. Blockade of CLEVER-1 restrains immune evasion and enhances anti-PD-1 immunotherapy in gastric cancer. J Immunother Cancer. 2025;13.
52. Hollmén M, Figueiredo CR, Jalkanen S. New tools to prevent cancer growth and spread: a 'Clever' approach. Br J Cancer. 2020;123:501–09.
53. Virtakoivu R, et al. Systemic blockade of clever-1 elicits lymphocyte activation alongside checkpoint molecule downregulation in patients with solid tumors: results from a phase I/II clinical trial. Clin Cancer Res. 2021;27:4205–20.
54. Rannikko JH, Bono P, Hynninen J, Hollmén M. Bexmarilimab activates human tumor-associated macrophages to support adaptive immune responses in interferon-poor immune microenvironments. Cancer Immunol Res. 2024;12:48–59.
55. Rannikko JH, et al. Macrophage sensitivity to bexmarilimab-induced reprogramming is shaped by the tumor microenvironment. J Immunother Cancer. 2025;13:e011292.
56. Sharma P, Hu-Lieskovan S, Wargo JA, Ribas AP. Adaptive, and acquired resistance to cancer immunotherapy. Cell. 2017;168:707–23.
57. Cassetta L, Kitamura T. Macrophage targeting: opening new possibilities for cancer immunotherapy. Immunology. 2018;155:285–93.
58. Palani S, Elima K, Ekholm E, Jalkanen S, Salmi M. Monocyte stabilin-1 suppresses the activation of Th1 lymphocytes. J Immunol Baltim Md 1950. 2016;196:115–23.
59. Karikoski M, et al. Clever-1/stabilin-1 controls cancer growth and metastasis. Clin Cancer researchoff J Am Assoc Cancer Res. 2014;20:6452–64.